American Mineralogist, Volume 89, pages 1228–1239, 2004

Experimental studies on the formation of porous gas hydrates

GEORGI GENOV,[1,*] WERNER F. KUHS,[1] DOROTEYA K. STAYKOVA,[1] EVGENY GORESHNIK,[1] AND ANDREY N. SALAMATIN[1,2]

[1]GZG Abt. Kristallographie, Georg-August-Universität Göttingen, Göttingen 37077, Germany
[2]Department of Applied Mathematics, Kazan State University, Kazan 420008, Russia

ABSTRACT

Gas hydrates grown at gas-ice interfaces were examined by electron microscopy and found to have a sub-micrometer porous structure. In situ observations of the formation of porous CH_4- and CO_2-hydrates from deuterated ice Ih powders were made at different pressures and temperatures, using time-resolved neutron diffraction data from the high-flux D20 diffractometer (ILL, Grenoble) as well as in-house gas consumption measurements. The CO_2 experiments conducted at low temperatures are particularly important for settling the open question of the existence of CO_2 hydrates on Mars. We found that at similar excess fugacities, the reaction of CO_2 was distinctly faster than that of CH_4. A phenomenological model for the kinetics of the gas hydrate formation from powders of spherical ice particles is developed with emphasis on ice-grain fracturing and sample-consolidation effects due to the outward growth of gas hydrate. It describes (1) the initial stage of fast crack-filling and hydrate film spreading over the ice surface and the two subsequent stages which are limited by (2) the clathration reaction at the ice-hydrate interface and/or by (3) the diffusive gas and water transport through the hydrate shells surrounding the shrinking ice cores. In the case of CO_2-hydrate, the activation energies of the ice-surface coating in stage 1 are estimated to be 5.5 kJ/mol at low temperatures and 31.5 kJ/mol above 220 K, indicating that water molecule mobility at the ice surface plays a considerable role in the clathration reaction. Comparable activation energies of 42.3 and 54.6 kJ/mol are observed in the high temperature range for the reaction- and diffusion-limited stages 2 and 3, respectively.

INTRODUCTION

Gas clathrate hydrates are non-stoichiometric inclusion compounds encaging small, usually apolar guest molecules in a host-framework of hydrogen bonded water molecules. They exist as a stable solid phase at high gas pressures and/or low temperatures (van der Waals and Platteeuw 1959). Two main crystallographic structures of gas hydrates, the von Stackelberg cubic structures I and II, are distinguished, both consisting of two types of cavities, small and large cages, that can be occupied by guest molecules (Sloan 1998). It is generally assumed that the encaged gas molecules cannot exchange with the environment after formation. Rather, the guest molecules have to be built into the crystal structure during the growth process according to their chemical activity at the reaction site.

Since the 1950s, many gas hydrate systems have been studied. Still, some physico-chemical properties of gas hydrates as well as their formation and decomposition kinetics are neither well known nor properly understood, though they are of primary importance for several reasons (Sloan 1998). With traces of water in gas and oil transport systems hydrate stability conditions are met leading eventually to complete blockages of pipelines. Likewise, the kinetics of CH_4-hydrate formation and decomposition is of major significance in geological settings, for our understanding of the role of methane gas in climate change, for the possible use of natural gas hydrate deposits as a future source of energy, or simply for a more economic transport and storage of gas. CO_2 clathrate hydrates could also be a possible way to sequester CO_2 into the ocean to reduce global warming (Warzinski et al. 2000). They may also play a major role in some terra-forming processes on Mars (Cabrol et al. 1997; Komatsu et al. 2000; Wilson and Head 2002). In addition, they could affect the rheological properties of the polar ice layers at the north and south Martian poles (Brightwell et al. 2003; Durham 1998; Kargel 1998; Kargel and Tanaka 2002; Kreslavsky and Head 2002; Milkovich et al. 2002). Moreover, the higher the amount of CO_2 hydrate in the caps, the longer the period needed for establishing a steady-state geothermal gradient in their inner parts, which would affect basal melting (Kargel and Tanaka 2002; Kreslavsky and Head 2002). Not much is known about the formation kinetics of CO_2 hydrates under Martian conditions, and the present work partly intends to establish a solid physico-chemical basis for the hypotheses listed above. In this context, the most relevant formation process is the reaction of ice Ih with CO_2 gas to hydrate. A strong dependence of the transformation rates on the surface area of the gas-ice contact was demonstrated by Barrer and Edge (1967). Later, Hwang et al. (1990) studied methane-hydrate growth on ice as a heterogeneous interfacial phenomenon and measured the clathrate formation rates during ice melting at different gas pressures. Sloan and Fleyfel (1991) discussed molecular mechanisms of the hydrate-crystal nucleation on ice surfaces, emphasizing the role of the quasi-liquid-layer (QLL). Takeya et al. (2000) made in situ observations of CO_2-hydrate

* E-mail: ggenov@gwdg.de

0003-004X/04/0809–1228$05.00

growth from ice-powder for various thermodynamic conditions using laboratory X-ray diffraction. They distinguished the initial ice-surface coverage stage and a subsequent stage, which was assumed to be controlled by gas and water diffusion through the hydrate shells surrounding the ice grains. This process was modeled following Hondoh and Uchida (1992) and Salamatin et al. (1998) with a single ice particle approximation. The respective activation energies of the ice-to-hydrate conversion were estimated as 0.2 and 0.4 eV (19.2 and 38.3 kJ/mol). The first in situ neutron diffraction experiments on kinetics of clathrate formation from ice-powders were presented by Henning et al. (2000). They studied CO_2-hydrate growth on D_2O ice Ih, using the high intensity powder diffractometer HIPD at Argonne National Laboratory at temperatures ranging from 230 to 263 K and at a gas pressure of approximately 900 psi (6.2 MPa). The starting material was crushed and sieved ice with unknown but most likely irregular grain shapes. To interpret their results at a later stage of the hydrate formation process, the authors applied a simplified diffusion model for flat hydrate-layer growth, developed for the hydration of concrete grains (Berliner et al. 1998; Fujii and Kondo 1974), and obtained an activation energy of 6.5 kcal/mol (27.1 kJ/mol). This work was continued by Wang et al. (2002), who studied the kinetics of CH_4-hydrate formation on deuterated ice particles. A more sophisticated shrinking ice-core model (Froment and Bischoff 1990; Levenspiel 1999) reduced to the diffusion model of Takeya et al. (2000, 2001) was used to fit the measurements. A higher activation energy of 14.7 kcal/mol (61.3 kJ/mol) was deduced for methane hydrate growth on ice. Based on Mizuno and Hanafusa (1987), the authors suggested that the quasi-liquid layer of water molecules at the ice-hydrate interface may play a key role in the (diffusive) gas and water redistribution although a definite proof could not be given.

One of the recent and most intriguing find is that, at least in cases where the guest species are available as excess free gas, some gas hydrate crystals grow with a nanometric porous microstructure. Using cryo field-emission scanning electron microscopy (FE-SEM), direct observations of such sub-micrometer porous gas hydrates have now been made (Klapproth 2002; Klapproth et al. 2003; Kuhs et al. 2000; Staykova et al. 2002, 2003). Hwang et al. (1990) reported that the methane hydrates formed from ice in their experiments were bulky and contained many voids. Rather interestingly, there is evidence that besides dense hydrates, some natural gas hydrates from the ocean sea floor also exhibit nanometric porosity (Suess et al. 2002). Based on experimental studies (Aya et al. 1992; Sugaya and Mori 1996; Uchida and Kawabata 1995) of CO_2 and fluorocarbon hydrate growth at liquid-liquid interfaces, Mori and Mochizuki (1997) and Mori (1998) proposed a porous microstructure for the hydrate layers between the two liquid phases and suggested a phenomenological capillary permeation model of water transport across the films. Although the general physical concepts of this phenomenon in different situations may be quite similar, we still do not have sufficient data to develop a unified theoretical approach to its modeling (Mori 1998). The study presented here is confined to the particular thermodynamic conditions of gas hydrate formation from ice in a single-component gas atmosphere at pressures well exceeding the dissociation pressure at constant temperatures below the quadruple point.

In accordance with numerous experimental observations (Henning et al. 2000; Kuhs et al. 2000; Staykova et al. 2002, 2003; Stern et al. 1998; Takeya et al. 2000; Uchida et al. 1992, 1994), a thin gas hydrate film rapidly spreads over the ice surface at the initial stage of the ice-to-hydrate conversion. This stage of surface coverage was labeled stage I in our previous publications (Staykova et al. 2002, 2003). Subsequently, the only way to maintain the clathration reaction is the transport of gas molecules through the intervening hydrate layer to the ice-hydrate interface and/or of water molecules from the ice core to the outer hydrate-gas interface. As mentioned above, diffusion-limited clathrate growth was assumed for this second stage as described by Takeya et al. (2000), Henning et al. (2000), and Wang et al. (2002) on the basis of the shrinking-core models formulated for a single ice particle, without taking explicit account of a surface coverage stage. However, in the case of porous gas hydrates, gas and water mass transport through the hydrate layer becomes much easier, and the clathration reaction itself together with the gas and water transfer over the phase boundaries may be the rate-limiting step(s) that follows the initial coverage. This process should be modeled simultaneously with the ice-grain coating (Salamatin and Kuhs 2002). We have labeled this reaction-limited stage as stage II. Certainly, we can still expect the onset of a diffusion-limited stage (stage III in our nomenclature) of the hydrate formation process completely or, at least, partly controlled by gas and water diffusion through the hydrate phase, especially when a highly consolidated ice-hydrate structure develops with thick and dense hydrate shells surrounding ice cores and/or when the nanometric porosity is predominantly closed. As a result, the hydrate-phase growth and expansion beyond the initial ice-grain boundaries into the sample voids and the corresponding reduction of the specific surface of the hydrate shells exposed to the ambient gas can be a principal factor which slows down the hydrate formation rates at the later stages of the clathration reaction, as predicted by Staykova et al. (2003).

Here, we continue previous studies presented in Salamatin and Kuhs (2002) and Staykova et al. (2002, 2003) and attempt to quantitatively describe all the subsequent stages of the formation process of CH_4 and CO_2 gas hydrates as followed by in situ neutron diffraction and gas consumption experiments, starting from a well-characterized ice powder of known structure, grain size, and specific surface area. While neutron experiments give unique access to the fast initial part of the clathration reaction, in-house gas consumption experiments are indispensable for the much slower later stages of hydrate formation. Together with our kinetic diffraction studies, ex situ FE-SEM observations of the formation of porous gas hydrates proved to be helpful in understanding the initial coating phenomenon and the evolution of ice-powder structure during the clathration reaction and to construct a phenomenological multi-stage model of gas hydrate growth from ice powders. In particular, recent SEM images clearly show that the clathration reaction often starts in cracks of the ice grains formed during the preparation of the starting material. Thus, special attention will be paid here to the crack-filling sub-stage, which precedes or accompanies coverage of the spherical ice grain surfaces. A model for crack-filling is presented here for the first time and is applied to fit and interpret the experimental data.

EXPERIMENTAL METHODS AND SAMPLE PREPARATION

Diffraction instrumentation and gas-consumption technique

Neutron diffraction techniques are well suited to investigate gas hydrate formation kinetics as the strong penetration of neutrons allows for the use of thick-walled high-pressure gas equipment for cryogenic devices. We performed in situ neutron diffraction experiments at various pressures and temperatures with CH_4 and CO_2 gas on the high-intensity 2-axis D20 neutron diffractometer at ILL, Grenoble. D20 is a medium to high-resolution diffractometer providing a high flux at the sample position. It has 1536 detection cells in a stationary, curved linear position sensitive detector (PSD) covering a 2θ range of 153.6°. This makes D20 an ideal tool for in situ diffraction studies with acquisition times under one second, which makes it possible to follow fast changes in the sample. More details about the instrument can be found at http://www.ill.fr/YellowBook/D20 and in Convert et al. (1998, 2000).

The beam-time allocation of neutron sources is typically limited to a few days. Therefore, the reaction kinetics at longer time scales can not usually be investigated by in situ neutron diffraction. At lower temperatures in particular, the reaction can take several weeks to several months. Therefore, we have also designed and employed an in situ technique based on gas consumption during the formation reaction. Different arrangements are used for pressures above and below 0.1 MPa shown in Figures 1 and 2 respectively. Using a gas pressure cell made of a high-strength aluminum alloy with a typical volume of 2 cm^3 and a low-temperature bath, the reaction is followed by recording the drop of gas pressure in the system. The pressure in the system is adjusted manually from time to time in order to maintain the pressure within typically a few percent fraction of the target pressure. As the pressure drop depends on the amount of ice in the pressure cell as well as on the free gas volume of the specific arrangement, calibration is necessary at the end of each experiment. This is achieved by measuring the ratio of unreacted ice Ih to newly formed gas hydrate by means of X-ray powder diffraction. As laboratory X-ray sources lack the penetration power to allow for in situ measurements, the samples are recovered at liquid nitrogen temperatures and investigated at 80 K in a custom-made Philips MRD diffractometer equipped with an APD helium closed-cycle cryostat. The measured X-ray pattern is then analyzed using a full pattern Rietveld refinement technique with GSAS (Larson and von Dreele 1990). Occasional checks with samples measured previously by in situ neutron diffraction confirmed the reliability of the recovery method.

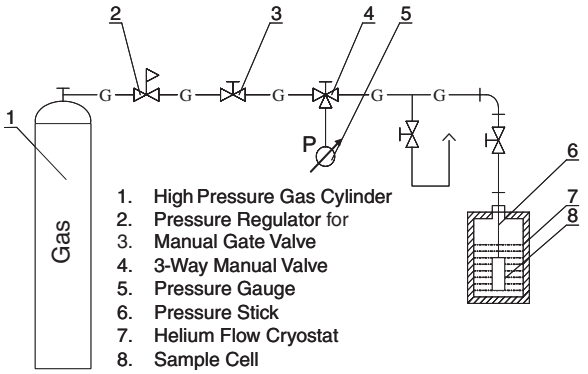

FIGURE 1. Schematic drawing of the set up for gas consumption measurement (>0.1 MPa)

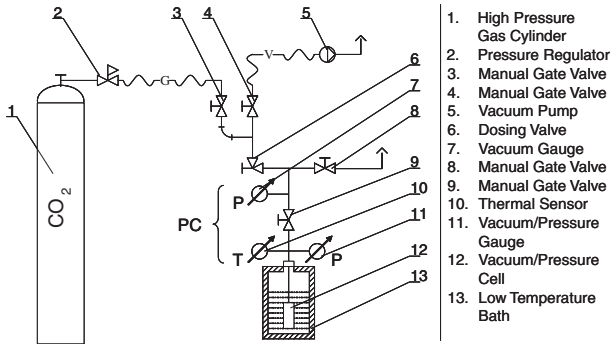

FIGURE 2. Schematic drawing of the set up for gas consumption measurement (<0.1 MPa)

Sample preparation

Spherical D_2O ice Ih grains with a typical diameter of several tens of μm were prepared (see Fig. 3a) in our laboratory in Götingen using a spraying technique. In order to quantify the morphology of the starting material, a representative part of the sample was investigated by FE-SEM. The pictures obtained were used to estimate the size distribution of the ice spheres. Measurements on different batches showed that the size distribution of ice spheres sprayed with the same nozzle is well reproducible and has a lognormal shape. The mean radius has been determined as 27 μm with a relative standard deviation of 0.8; for the first neutron experiment at 272 K ice spheres with a larger radius of 38.5 μm were used. The main characteristics of the ice samples and gas hydrates are presented in Table 1.

For the neutron diffraction experiments the samples were poured into thin-walled Al cans and transported in a dry-N_2 dewar to ILL/Grenoble. The estimated initial macro-porosity of $\varepsilon_{n0} \approx 30$ 35% corresponds to a packing density of about 65 70% in the Al cans. Two high-strength auto-frettaged aluminum gas pressure cells were manufactured in Götingen and adapted to an ILL sample holder. Temperature readings were obtained from a calibrated sensor fixed to the pressure cell wall. The Al cans were inserted into the pressure cell, already attached to the sample holder, and the Bridgman seal was closed. This filling operation was performed with a small stream of gas to ensure complete filling of the system. Subsequently, the pressure cell was inserted into the cryostat and the temperature was equilibrated at the chosen value. The desired gas pressure was applied within a few seconds while data collection was initiated. In our experiments, we did not observe an induction time except for temperatures below 200 K; reactions at higher temperatures began immediately (within the diffractometer time-resolution of a few seconds) after application of gas pressures higher than the decomposition pressure.

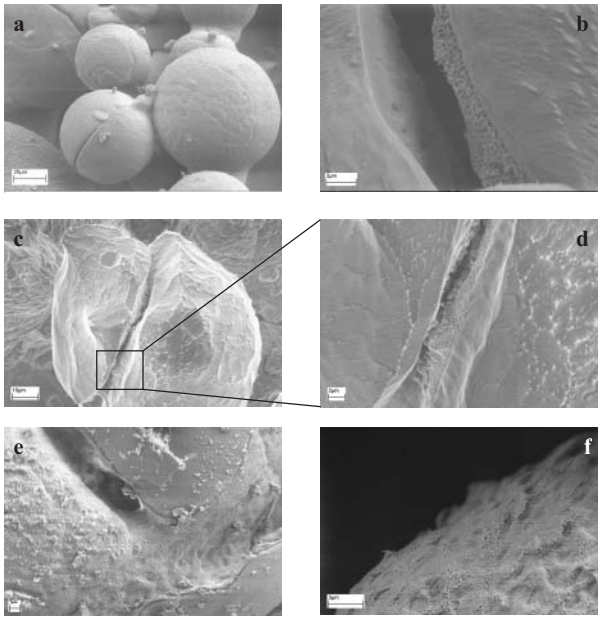

FIGURE 3. Field-emission scanning electron images of the starting ice-Ih material as well as samples quenched at various stages of the CO_2-hydrate formation process: (**a**) initial ice-Ih material, consisting of spheres with average diameter of 40–60 μm; (**b**) CO_2 hydrate formation on crack surface after 3 h of reaction at 193 K and 0.05 MPa; (**c**) view of a crack and a higher-magnification view into the crack (**d**) showing the crack surface coverage under the same conditions after 8 h of reaction; (**e**) reaction which started in the crack and spread over the grain surface (185 K, 0.036 MPa, 21 h); (**f**) surface coverage on a deuterated ice sphere after 52 min of reaction at 3 MPa and 275 K.

TABLE 1. Characteristics of ice samples and gas hydrates

Parameters and denotations	Values
Ice samples	
Ice density ρ_i, kmol/m^3	51
Typical (mean) grain size r_{i0}, µm	25–40
Relative standard deviation of grain radii	0.8
Specific surface area S_{i0}, m^2/mol	1.5–2.1
Average crack opening angle β, rad	0.06
Macro-porosity ε_{m0}	0.33
Coordination number Z_0	7
Random density slope of particle distribution C	15.5
Gas hydrates	
Water density in hydrate phase ρ_{hw}, kmol/m^3	45
Sub-micrometer porosity of CH_4– (CO_2–) hydrates ε_h	0.15 (0.1)

Diffractometer data collection and processing

To observe changes in the diffraction patterns during gas hydrate formation we used D20 at its highest intensity setting and a wavelength of $\lambda = 2.414$ Å. The reaction of gas (at constant pressure and temperature) with the ice grains was followed over a period of typically 10 to 20 h. The data presented here were collected with a time resolution of 30 s or 1 min for the initial fast reaction and with a resolution of 5 min for the slower later part of the reaction. In this way data of good statistical precision were obtained, suggesting that even times of several seconds would deliver useful information. An efficiency correction and a background subtraction were applied to all data. Subsequently, the measurements were analyzed with the GSAS Rietveld refinement program (Larson and von Dreele 1990), which gave quantitative information on the amount of gas hydrate formed as a function of time with an accuracy of about 0.1%. A two-phase (ice Ih + gas hydrate) Rietveld fit of the powder diffraction pattern obtained for each time interval was performed. Refined parameters were the lattice constants for ice Ih and gas hydrate, the phase fractions, and five to six background parameters; the scale factor and absorption coefficient were fixed. The atomic positions and displacement parameters for D_2O ice Ih and CH_4- or CO_2-hydrate phases were taken from Klapproth (2002) and were also kept fixed. The weight fraction of the clathrate phase α (mole fraction of ice converted to the gas hydrate) was extracted from the refinement for each time interval and was plotted as a function of time.

FE-SEM observations and SSA measurements

We restrict our phenomenological model developed in the theoretical section below to previous (Klapproth 2002; Klapproth et al. 2003; Kuhs et al. 2000; Staykova et al. 2002, 2003; Suess et al. 2002) as well as recent ex situ FE-SEM observations of porous gas hydrates recovered at various stages of the formation process. From a few hundred electron micrographs we have selected typical examples of the early stages of the reaction shown in Figure 3. Additionally, measurements of the specific surface area (SSA) of the starting material and partly reacted samples were made (Kuhs et al. 2004) using a BET adsorption method originally developed for SSA measurements of snow (Legagneux et al. 2002, 2003) in order to check the extent to which the nanometric pores are interconnected. Based on these observations in combination with general physical and mechanical concepts, we can formulate the following statements: (1) The starting material (ice Ih powder) consists of spherical grains several tens of micrometers in diameter (Fig. 3a). The arrangement of the ice grains in the sample is close to a random dense packing with a packing porosity of about 30–35%. The measured specific ice surface indicates minimum contact areas between grains. The typical time scales of the heat and mass transfer processes in the ice-powder samples are small (~5–10 min). The temperature in the pressure cell is essentially uniform, and all substances and energy are rapidly redistributed within the open space of the sample volume. (2) The initial stage of crack-filling and ice-grain surface coverage by a gas hydrate film is clearly distinguished from the subsequent stage(s) of growth of the hydrate shell into the shrinking isolated ice cores. Different mechanisms are generally involved in the coating process, such as preferential and relatively fast filling of cracks in the grains (Figs. 3b, 3c, and 3d), formation (nucleation) of hydrate patches on the ice surfaces, and lateral spreading of the hydrate film (Figs. 3e and 3f). At lower temperatures crack filling generally precedes surface coverage, while at temperatures above 230 K the surface coverage becomes more rapid and usually overlaps with filling of the cracks. Subsequently the porous gas hydrate shell grows and covers the ice surface to a large extent, leading to a consolidated sample in which the original ice grain structure can still be recognized. The intermediate stage II is thought to be limited by the clathration reaction (including gas and water redistribution across the phase boundaries) while stage III is assumed to be influenced (or fully controlled) by water- and gas-mass transport through the hydrate layers from and to the inner parts of the original ice grains, respectively. (3) The SSA measurements show increasing SSA, mainly during the surface coverage stage I until it reaches a limiting value, which suggests that the porosity is only partly open over a scale of a few micrometers. Hence, it is likely that only the initial hydrate film spreading over the ice-grain surface retains a high permeability. The time scale of the coating process ranges from several hours to several days, depending on thermodynamic conditions (see also section 4). As the thicker clathrate layers develop further, the pores (at least partly) lose their interconnectivity inside the hydrate at longer distances. Therefore, mass transport at the later stages of the clathration reaction cannot be achieved via the predominantly closed sub-micrometer pores. Rather, it must occur by bulk diffusion. Stages II and III can be observed in the FE-SEM only after breaking the consolidated sample to provide some inner surfaces. (4) All our FE-SEM pictures show that the hydrate crystallites grown from ice are rather small (from a few to some tens of mircometers). Typically, single crystals of hydrates have an isotropic, porous structure with a mean pore size on the order of several hundred nm for CH_4-, Ar-, and N_2- (*macropores* in the generally accepted terminology of porous materials), and several tens of nm for CO_2-hydrate (*mesopores* in this terminology), although non-porous gas hydrates are also observed in our SEM micrographs. There is no obvious dependency of the pore size on either pressure and temperature or on the time of reaction. From the SEM photographs, the internal meso- to macro-porosity of the hydrate phase is visually estimated as 10–20%. The diffraction data suggest a good crystallinity of the hydrate crystals, indicating a coherent "inward" growth of the hydrate shells without any appreciable deformation. This is also confirmed by the FE-SEM pictures, which show that the growth process generally does not perturb the initial setting of crystallites. (5) The density of water in the crystalline hydrate lattice of both types I and II is noticeably less than that of ice. Thus, the excess water molecules must be partly "evacuated" from the ice-hydrate contact area to provide additional space for the newly formed porous clathrate hydrates. This water (~20–30%) is transported toward the outer hydrate surface where it reacts with the ambient gas, leading to expansion of the hydrate layer into the open space between the initial ice grains and to a reduction of the pore surface area between them (see Figs. 3c–f). However, specific surface area measurements (see above) indicate that the total area of the gas hydrate interface does not decrease with time during the initial stage of the reaction. Consequently, as also confirmed by SEM micrographs, some of the nanometric porosity in the hydrates remains open. The higher the mean size of the ice grains, the less complete is the ice-to-hydrate transformation in a given time, presenting further evidence that thick hydrate layers gradually lose some of their permeability and/or closure of the open voids between the original ice grains occurs. The final consolidated stage is clearly born out by the compact nature of the product with irregular shapes of the ice-hydrate particles and little open pore space visible in the FE-SEM after breaking the sample.

THEORY

Principal notions

Because a clear molecular picture of the clathrate formation process is lacking, the primary goal of our study is the development of a phenomenological model for the different, partially overlapping stages of the clathration reaction in order to interpret the experimental kinetic data. In accordance with recent observations, ice spheres in the starting material may have cracks (see Figs. 3c and 3d) most probably caused by thermal strains which arise during ice-powder preparation by means of water droplets freezing in liquid nitrogen. Therefore, we continued our previous work (Salamatin and Kuhs 2002; Staykova et al. 2003) and additionally introduced a description for the crack-filling part of the initial surface coverage, which appeared in our FE-SEM micrographs as the prominent first step of the clathration reaction, especially at lower temperatures. Following Staykova et al. (2003), the geometry of the ice-powder structure is described in a monosize (or monodisperse) approximation, in terms of the mean-volume ice grain (core) radius r_i and the specific surface area of ice grains (cores) per mole of water molecules S_i (with

r_{i0} and S_{i0} indicating initial values). The degree of the reaction (the mole fraction of ice converted to hydrate phase) α is the principal characteristic of the hydrate formation process developed in time t. Correspondingly, the total crack-void fraction of ice grains in a sample is designated as ε_f, and the degree of crack-volume-filling in ice spheres of an initial radius of r_{i0} is χ. Hereinafter, we consider ε_f to have values of ~0.01–0.03.

Some of the ice grains in the sample may be connected by bonds. Nevertheless, in accordance with our observations, we assume that S_{i0} is equal to the sum of the spherical grain surfaces and, by definition,

$$S_i = \frac{3r_i^2}{\rho_i r_{i0}^3}, \ldots . \alpha = \frac{1}{1-\varepsilon_f}\left[\left(1-\frac{r_i^3}{r_{i0}^3}\right)\left(1-\varepsilon_f\frac{1+E}{E}\right)+\chi\frac{\varepsilon_f}{E}\right] \quad (1)$$

Here ρ_i is the molar density of ice. The hydrate-phase expansion coefficient E is the proportion of the hydrate volume excess with respect to the consumed ice volume

$$E = \frac{\rho_i}{\rho_{hw}\left(1-\varepsilon_h\right)} - 1$$

expressed via the mole density of water ρ_{hw} in hydrate and mesoporosity ε_h of the clathrate phase.

In accordance with Equation 1, the problem of modeling the gas-hydrate formation (reaction degree α) from monosize-sphere powders is reduced to a mathematical description of the principal parameters r_i and χ of a reference grain among densely packed identical neighbors with a given crack-volume fraction. The monodisperse approximation of the ice-sample structure was shown by Staykova et al. (2003) to be quite appropriate for the initial period of hydrate formation ($\alpha < 0.3$–0.4) until the volumetric expansion and geometric interaction of the growing hydrate shells become principal factors controlling the reaction rate. In this case, the extension of the theory to polydispersed powders with an experimentally well-established log-normal distribution of ice-sphere radii is rather straightforward: expression 1 for S_i should be additionally divided by the factor $1 + \sigma_0^2$, where $\bar{\sigma}_0$ is the relative standard deviation of the grain size. The general model for hydrate formation from polydisperse powders of randomly packed ice spheres valid for the later part of the reaction will be presented elsewhere.

Ice-core model

Now, we introduce (after Staykova et al. 2003) the rate of the ice sphere surface-coating ω_S and the rate of subsequent volume ice-to-hydrate transformation ω_V outside of cracks. The former quantity can be defined as the fraction of the open (exposed to the ambient gas) ice surface which becomes covered by the initial hydrate film (hydrate patches) during a unit time period, while the latter is the number of ice moles transformed to hydrate phase per unit of time on a unit area of ice surface after coating. We also designate as δ_0 the thickness of the ice layer converted in the coating process relative to the initial hydrate film of thickness $d_0 = \delta_0(1 + E)$. Parameter δ_0 (and d_0) is small compared to the mean grain size r_{i0}, whereas the rate of the initial hydrate film formation is assumed to be much higher than that of the hydrate layer growth on the coated surface ($\omega_S >> S_{i0}\omega_V$). Thus, the ice surface area remains practically constant ($S_i \approx S_{i0}$) during stage I.

Consequently, in accordance with Salamatin and Kuhs (2002), the radius of the shrinking ice core r_i in the sample is governed by the following mass balance equation

$$\frac{\mathrm{d}}{\mathrm{d}t}\left(1-\frac{r_i^3}{r_{i0}^3}\right) = S_i\left[\rho_i\delta_0\omega_S e^{-\omega_S t} + \omega_V(1-e^{-\omega_S t})\right] \quad (2a)$$

or, identically, in monodisperse approximation for S_i given by Equation 1

$$\frac{\mathrm{d}r_i}{\mathrm{d}t} = -\delta_0\omega_S e^{-\omega_S t} - \frac{\omega_V}{\rho_i}\left(1-e^{-\omega_S t}\right). \quad (2b)$$

The driving force of the hydrate formation is the supersaturation of the gas-ice-hydrate system, $\ln(f/f_d)$, expressed via fugacities f and f_d of the gaseous phase and decomposition pressures p and p_d at a given temperature T. For each stage, this driving force determines the clathration kinetics and contributes to the different steps in the ice-to-hydrate conversion in proportion to their apparent resistances, namely, k_S^{-1} for the initial hydrate film spreading over the ice surface, and k_R^{-1} and k_D^{-1} for the clathration reaction and gas/water permeation through the hydrate layer, respectively.

Hence, we conventionally write

$$\omega_S = k_S \ln\frac{f}{f_d}, \quad \omega_V = \frac{k_R k_D}{k_R + k_D}\ln\frac{f}{f_d} \quad (3)$$

Depending on the rate-limiting step of the hydrate formation process, ω_V describes either the rate of the clathration reaction (ω_R) in stage II (when $k_D >> k_R$) or the rate of gas and water mass transfer through the hydrate shell (ω_D) in stage III (when $k_D << k_R$). For comparable values of k_R and k_D in the latter part of Equation 3, both steps are important.

The clathration rate constants are assumed to be the Arrhenius-type functions of temperature:

$$k_J = k_J^* \exp\left[\frac{Q_J}{R_g}\left(\frac{1}{T_*}-\frac{1}{T}\right)\right], \quad J = S, R, D, \quad (4)$$

where k_J^* and Q_J are the clathration rate constant at the reference temperature T_* and the activation energy of the J-type step; R_g is the gas constant.

Phenomenological Equations 1–4 are considered to be a theoretical basis for the detailed analysis of the different stages of hydrate formation and interpretation of the neutron diffraction data. Actually, each J-th step, explicitly presented in the model, may be further divided into a sequence of substeps characterized by their own resistances, the sum of which is k_J^{-1}. Nevertheless, for a fixed temperature k_S and k_R can still be used as tuning parameters, but the permeation rate constant k_D depends on geometrical characteristics of the hydrate layers growing around shrinking ice cores and must be related to r_i to complete Equations 2 and 3.

Permeation resistance of the hydrate layer

Here we follow the geometrical description of powder-particle growth developed by Arzt (1982) for a random dense packing of monodisperse spheres on the basis of the concept of Voronoi cells associated with the initial powder structure. The build-up of the starting material is characterized by the average

number of contacts per particle (coordination number) Z_0 and the relative slope C of the random packing density function. Experimental estimates for these parameters deduced by Arzt (1982) are given in Table 1 and are consistent with the observed porosity of our ice-powder samples.

As shown schematically in Figure 4, the shape of each hydrate layer formed from a single spherical ice grain is represented as a truncated sphere of radius r_h. The ice core shrinks, and its radius r_i decreases due to inward growth of the hydrate layer. However, because of the lesser density of water in the porous hydrate phase, the excess water molecules must be transported to the outward hydrate surface exposed to the ambient gas, and the hydrate layer simultaneously expands into the open space between the original ice grains, eventually filling most of the initial open space. The existing contact areas between neighboring hydrate shells (ice-hydrate particles) increases and additional contacts are formed as r_h grows. Correspondingly (see Appendix A for details), the fraction s of the free hydrate surface area exposed to the ambient gas, the specific surface area of the macro-voids S_m, and the macro-porosity of the sample ε_m decrease. Finally, the current sample geometry is related to the ice core radius r_i by means of the hydrate-volume expansion factor E.

The fictitious spherical boundary of radius r in Figure 4 divides the hydrate shell into two sub-layers 1 and 2: from r_i to r and from r to r_h, respectively. The permeation (diffusion) resistance of the spherical sub-layer 1 is known from diffusion theory (Crank 1975). To estimate the resistance of the truncated sub-layer 2, we assumed (Staykova et al. 2003) that locally the mass-transfer process in the layer is similar to diffusion through a concave spherical layer of the same thickness with the same total areas of bounding surfaces. Finally, we arrived at the following relation for the permeation rate constant in Equation 3:

$$k_D = \frac{\rho_i D}{r_{i0}}\sigma, \quad \sigma = \frac{\sqrt{s}R_h R}{R_i\left[\sqrt{s}R_h\left(R - R_i\right) + R_i\left(R_h - R\right)\right]} \tag{5}$$

Here D is the apparent gas/water mass transfer (permeation) coefficient proportional to that introduced in Salamatin et al. (1998), and σ is the complex geometrical characteristic of the developing sample structure expressed via normalized parameters $R = r/r_{i0}$, $R_i = r_i/r_{i0}$, and $R_h = r_h/r_{i0}$. The temperature dependence of the permeation coefficient follows Equation. 4 with k_D^* corresponding to D^* at the reference temperature T^* in Equation 5.

If the expansion effect is neglected ($E = 0$), the hydrate shells in the sample remain within the initial ice-grain boundaries, R_h and s equal unity, and Equation 5 is reduced to the diffusive shrinking-core model for a single particle employed by Takeya et al. (2000) and Wang et al. (2002). Actually, in the case of a dense packing of the ice-powder, such an approximation might be valid only in the very beginning of the hydrate formation process when $R_h - R_i \to 0$ in Equations 5 and $\sigma \to \infty$ (i.e., $k_D \to \infty$). Consequently, in accordance with Equations 2 and 3, the kinetics of the ice-to-hydrate conversion passes, at least initially, through stages I and II as controlled by the ice surface coverage process and/or by the clathration reaction—and not by diffusion. Thus, the simplified models used in Henning et al. (2000), Takeya et al. (2000), and Wang et al. (2002) are neither applicable for an interpretation of the initial stage of the clathration reaction, nor are they valid for the final phase of sample consolidation.

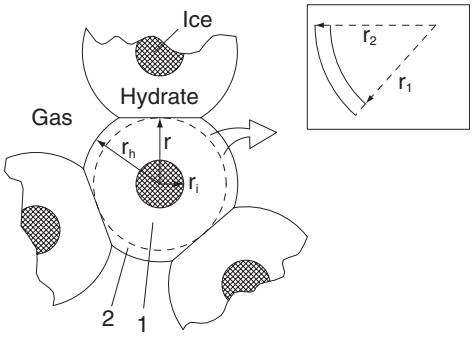

FIGURE 4. Schematic diagram of gas hydrate expansion into the voids between the ice spheres during the growth of hydrate shells around the shrinking ice cores. In the diffusion model (see text) the permeation resistance of the convex sub-layer 2 surrounding the inner spherical hydrate layer 1 is assumed to be similar to that of the concave spherical layer shown in the insert. See text for further details.

Gas hydrate growth in a crack of an ice grain

The fissures were in SEM images (see Figs. 3c and 3d) of the starting material (ice samples), although rather narrow, are open and usually penetrate deep into the powder particles. The observed process of fast initial hydrate growth in the ice-grain cracks, schematically shown in Figure 5, is assumed to develop simultaneously with the hydrate film patches spreading over the spherical surface of the reference grain as an independent, relatively short counterpart (sub-stage) of the initial stage I. To calculate the degree of volume-filling χ in a reference ice grain of initial radius r_{i0}, we write analogues of Equations 2 and 3 for hydrate formation on the crack surface (see Appendix B), designating all corresponding characteristics by primes. Thus, for example, the thickness δ_0' of the ice layer converted to the initial hydrate film spreading over the crack sides is introduced together with the respective rates ω_S' and ω_R' of the crack surface coating and clathration reactions, the latter being related to the temperature-dependent rate constants k_S' and k_R' with activation energies Q_S' and Q_R'. Then, as explained in Appendix B, for the mean crack-opening angle β the average height h of the crack-filling (see Fig. 5) normalized by r_{i0} can be explicitly expressed (at constant ω_R') vs. time t:

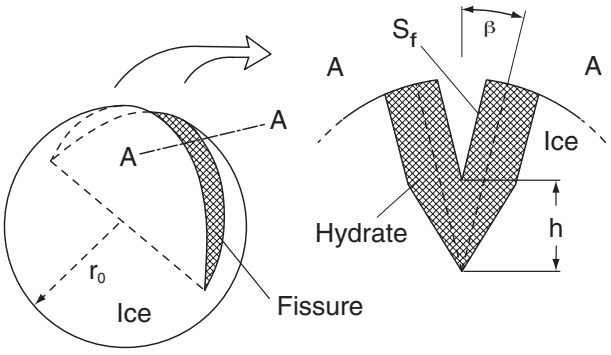

FIGURE 5. Schematic diagram of the hydrate formation in an ice-grain fissure and its A-A cross-section. The ice at the cleavage sides S_f is converted to hydrate at constant rate ω_R', and the height h linearly increases with time. See text for further details.

$$\xi = h/r_{i0} = A'\left(1-\mathrm{e}^{-\omega'_s t}\right) + B't\ ,\ \ h < r_0,$$
$$A' = \frac{E}{\beta r_{i0}}\left(\delta'_0 - \frac{\omega'_R}{\rho_i \omega'_S}\right),\quad B' = \frac{E\omega'_R}{\beta\rho_i r_{i0}}, \tag{6a}$$

until complete filling is reached at $h = r_{i0}$, i.e., $\xi = 1$.

The area S_f of each crack side exposed to the ambient gas decreases as the hydrate fills the fissure. The volume of hydrate growing in the crack is calculated in Appendix B by integration of the incremental mean hydrate layers with respect to h, which yields the degree of filling term χ in the following form:

$$\chi = \frac{3}{4}\pi\xi - \frac{3}{2}\xi\arcsin\xi - \frac{3}{2}\left(1-\xi^2\right)^{1/2} + \frac{1}{2}\left(1-\xi^2\right)^{3/2} + 1\ ,\ \xi < 1, \tag{6b}$$

and $\chi \equiv 1$ for $\xi > 1$.

Although this relationship is derived for a crack penetrating to the center of a reference grain, it has a general structure and after substitution of Equation 6_1 can be tuned to any lesser mean initial relative depth of cracks by appropriate correction of A' and B' (e.g., by β).

Qualitative analysis of the model

Solutions of the general models 1–6 can be obtained only numerically, but for fixed pressure and temperature conditions, during stages I and II, at least in the beginning of the clathration reaction when $k_D >> k_R$, quantities ω_S and ω_V given by Equation 3 can be considered as constant values ($\omega_V = \omega_R$), and Equation 2 can be integrated analytically. This yields an analogue of the asymptotic solution which was derived at $k_D \to \infty$ in Salamatin and Kuhs (2002).

$$r_i/r_{i0} = 1 - A(1 - \mathrm{e}^{-\frac{\omega_S}{\omega}t}) - Bt \tag{7}$$

where

$$A = \frac{\delta_0}{r_{i0}} - \frac{B}{\omega_S},\quad B = \frac{\omega_R}{r_{i0}\rho_i}$$

Parameter A is the difference of two small terms and, hence, its absolute value is expected to be small although the quantity itself can be either positive or negative.

Neglecting terms of the order of magnitude of $O(\varepsilon_f^2 / E^2)$ and combining the latter Equation 7 with Equations 1 and 6, one obtains a generalized asymptotic relation for the reaction-limited kinetics of the hydrate formation process valid for small values of α:

$$\left(1-\alpha\right)^{1/3} \approx 1 - \frac{\varepsilon_f}{3E}\chi\left(\xi\right) - A\left(1-e^{-\omega_S t}\right) - Bt\ . \tag{8}$$

As noted in Staykova et al. (2003), Equation 8 requires that the graph of $(1 - \alpha)^{1/3}$ vs. time t for the earlier phase of hydrate formation during stage II and limited by the clathration reaction for $t >> \omega_S^{-1}$ should be a straight line with slope B and intercept $1 - A - \varepsilon_f / (3E)$. This also gives us an insight into how the model parameters can be constrained by the kinetic measurements. First, via Equations 7 and 8, the asymptotic slope B is directly linked to the bulk ice-to-hydrate transformation rate and, for a given estimate for the grain-surface-coating rate ω_S, coefficient A (and, hence, δ_0) is determined, while ω_S can also be somewhat corrected so as to follow back in time the preceding adjacent part of the reaction data. Then, the intercept of curve 8 directly delivers the crack void fraction ε_f. Finally, parameters A' and B' (i.e., δ'_0 and ω'_R for a given estimate for ω'_S) in Equations 6 and 8 can be adjusted to fit the very beginning of the kinetic curve which is mainly affected by the crack-filling process. Due to the difference in time scales ($\omega'_S >> \omega_S$), the two sub-stages of the initial stage I are well distinguished, especially at low temperatures. The latter conclusion was demonstrated in Staykova et al. (2003), where a noticeable mismatch between Equation 7 and experimental data was observed at the very beginning of the clathration reaction (see Fig. 8 in this paper).

In the general case, the rate of the hydrate phase growth ω_V in Equations 2 and 3 may be significantly influenced or even limited by gas and water diffusion through the hydrate layer. Substitution of Equation 5 into the last part of Equation 3 yields

$$\omega_V = \omega_R\left(1 - \frac{1}{1+F\sigma}\right),\quad F = \frac{D\rho_i}{r_{i0}k_R}\ . \tag{9}$$

The dimensionless complex F in Equation 9 is the principal parameter responsible for the onset of stage III controlled (or influenced) by gas/water mass transfer through hydrate shells surrounding the shrinking ice cores. As explained above, the normalized factor σ changes from infinitely large values in the beginning of the clathration reaction to the first order of magnitude in the later phase of the gas hydrate formation. Thus, the ice-hydrate system can never pass to stage III at large F, and $\omega_V \approx \omega_R$ in Equations 3 and 9. For $F << 1$ stage II becomes extremely short and ends up, together with stage I, being directly replaced by the diffusion-limited stage III. The intermediate values of $F \sim 1$ correspond to the onset of stage III simultaneously controlled by both (reaction and diffusion) steps.

For the hydrate formation process influenced by gas and water transport through the hydrate layers, the time behavior of the quantity $(1 - \alpha)^{1/3}$ becomes non-linear. Correspondingly, after some time t^* in the beginning of the diffusion-limited stage III described (for small α) by the simplified diffusion theory of Fujii and Kondo (1974), the relative ice-core radius r_i/r_{i0} is proportional to $(t - t^*)^{1/2}$. More elaborate models (Salamatin et al. 1998; Takeya et al. 2000; Wang et al. 2002) predict even higher non-linearity due to the decrease in the ice-core surface S_i. However, they do not take into account the initial stage I, as well as the sample compaction and the reduction of the macro-pore surface S_m in the course of the ice-to-hydrate transformation, as described by Equation 5. The latter effects additionally suppress the gas and water fluxes through the hydrate shells to and from the ice cores and slow down the reaction. However, as shown by Staykova et al. (2003), the difference between the reaction- and diffusion-limited kinetics of hydrate formation becomes noticeable only at the final phase of the clathration reaction (for $\alpha > 0.5$–0.6). Before this, the α-curves can be equally well approximated by both limiting scenarios. Another peculiarity of the diffusion-limited conversion of ice powders to clathrate hydrates confirmed by Equations 1–3 and 5 and discussed in Staykova et al. (2003) is that the hydrate-growth rate in this case is inversely proportional to r_{i0}^2, being in contrast to the first two stages with A and B inversely proportional to r_{i0} in Equations 7 and 8. Thus, the stages controlled by different rate-limiting steps

(clathration reaction or gas/water transport through the hydrate shells) can be distinguished from each another. This may also help to recognize the formation of porous gas hydrates in the analysis of kinetic data.

As mentioned above, at the beginning of the hydrate formation process (for $\alpha < 0.3$–0.4) the monosize description of the ice-sample structure can be directly extended to polydispersed powders with log-normal distribution of ice-sphere radii. The necessary correction of Equation 1 for S_i presumes that the right-hand side of Equation 2_2 and coefficients A', B' and A, B in Equations 6, 7, and 8 should also be divided by the factor $1 + \bar{\sigma}^2_0$.

Results and discussion

CO_2-hydrate formation

Two series of in situ neutron diffraction experiments were previously conducted with D_2O-ice and a third one with H_2O-ice. Some of these results, in particular for methane, were presented in Staykova et al. (2003) where it was also shown that the deuterated and hydrogenated systems were essentially identical. Recently, a new series of in situ diffraction experiments with D_2O-ice as well as in-house measurements of CO_2-gas hydrate formation have been performed. Here we apply the model developed above to continue our study of hydrate formation from ice powders with special emphasis on crack filling during the initial stage I and CO_2-hydrate formation over a broad range of temperatures, including those related to Martian conditions (see Table 2).

In neutron-diffraction measurements, the gas hydrate growth reveals itself by an increase of the Bragg intensities originating from the gas hydrates which starts immediately after the application of gas pressure and increases with time while the amount of ice Ih decreases. The repeatedly reported induction period (Sloan 1998) was observed only at temperatures below 200 K and is not discussed here. A series of three experiments at 263, 253, and 230 K was performed with deuterated samples (see Fig. 6a). The reactions lasted between 17 and 26 h (see Table 2), resulting in 13 37% ice-to-hydrate conversion. An experiment performed with larger ice grains at 272 K (Fig. 6b) reported by Staykova et al. (2003) with a total reaction degree of about 56% was also used and is re-analyzed here. Likewise, the methane 230 K data up to 5%-degree transformation obtained previously (Staykova et al. 2003) have been re-examined with the improved model and are shown in Figure 6c along with the 230 K CO_2 data.

Another series of experiments were performed at 223, 203, and 193 K using our in-house gas consumption technique (described in section 2), also starting with deuterated ice. The reac-

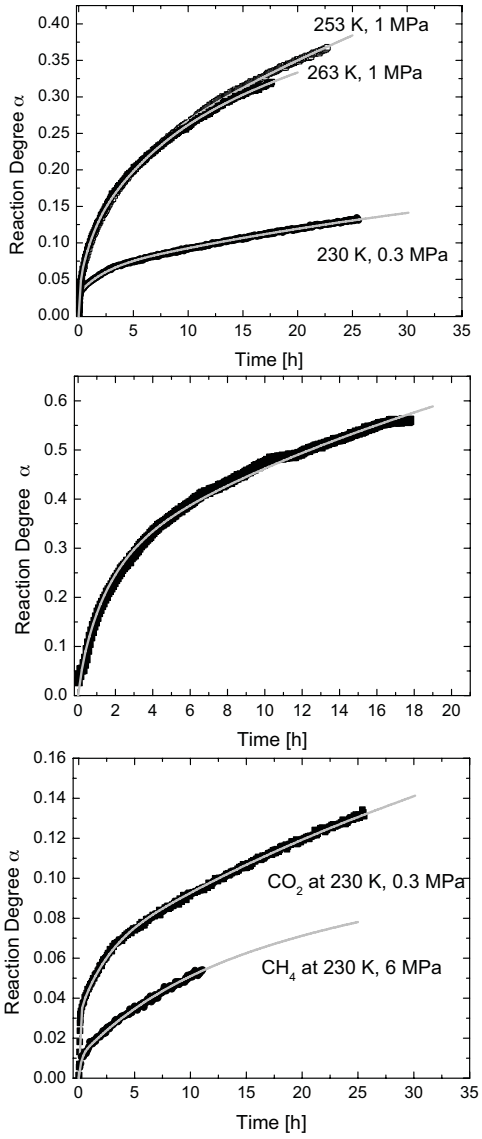

Figure 6. Plots of the data obtained during the neutron diffraction experiments, showing the temperature and pressure dependency of the growth kinetics: (**a**) comparison of the growth of CO_2 hydrate from deuterated ice under different thermodynamic conditions; (**b**) the most complete neutron kinetic experiment of CO_2 hydrate formation from deuterated ice at 272 K and 2 MPa; (**c**) comparison of the hydrate formation rates of CO_2 (0.3 MPa) and CH_4 (6 MPa) at 230 K. The light gray lines are the model fits.

Table 2. Conditions of experiments and kinetic parameters of gas hydrate formation

Conditions of experiments							Parameters of diffusion (D) and reaction (k_R) limited kinetics							
Ice	r_{i0}, µm	Gas	T, K	p (f), bar	p_d (f_d), bar	Time, h	k_S', 1/h	k_R', kmol/m² h	δ_0', µm	k_S, 1/h	k_R, kmol/m² h	D, m²/h	δ_0, µm	ε_f
		CH_4	230	60 (46.2)	5.9 (5.8)	11	2	$1.2\cdot10^{-5}$	1.4	$1.2\cdot10^{-2}$	–	–	1.6	$1.2\cdot10^{-2}$
				3 (2.9)	1.86 (1.82)	26	20	$2\cdot10^{-4}$	3.7	$8\cdot10^{-2}$	$2.6\cdot10^{-6}$	$1.4\cdot10^{-13}$	1–1.8	$1.5\cdot10^{-2}$
D_2O	27	CO_2	193	0.5 (0.495)	0.22 (0.219)	126	0.7	$7\cdot10^{-5}$	2.3	$2.2\cdot10^{-2}$	–	–	1.9	$1.8\cdot10^{-2}$
			203	0.89 (0.88)	0.433 (0.43)	48	5	$2.3\cdot10^{-4}$	2.3	$2.7\cdot10^{-2}$	–	–	1.9	$1.8\cdot10^{-2}$
			223	1.95 (1.9)	1.3 (1.28)	239	1.8	$(0.85–1.5)\cdot10^{-4}$	2.3	$3.5\cdot10^{-2}$	$3.7\cdot10^{-7}$	$1.9\cdot10^{-14}$	1.4	$(1.6–1.9)\cdot10^{-2}$
			253	10 (9.1)	5.1 (4.9)	22.5	20	$4\cdot10^{-4}$	3.3	0.35	$1.4\cdot10^{-5}$	$1.5\cdot10^{-12}$	2.2–3.4	$1.6\cdot10^{-2}$
			263	10 (9.3)	7.5 (7.1)	17.5	30	$8\cdot10^{-4}$	3.3	0.49	$1.9\cdot10^{-5}$	$2\cdot10^{-12}$	3.5–4.2	$2.2\cdot10^{-2}$
	38.5		272	20 (19.7)	11.4 (11.3)	18	5	$4\cdot10^{-5}$	3.3	0.85	$3.5\cdot10^{-5}$	$6.4\cdot10^{-12}$	4–5.6	$(1.6–1.8)\cdot10^{-2}$

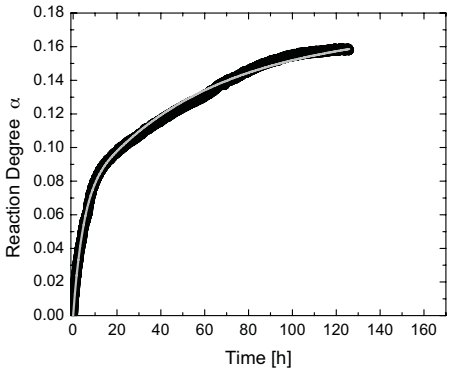

FIGURE 7. CO_2 hydrate formation reaction at 193 K and 0.5 MPa performed by the *pVT* method (see Fig. 2). The light gray line is the model fit.

tion degree did not exceed 17%. All these experiments covering the temperature range from 193 to 272 K were used to obtain the tuned model parameters listed in Table 2; examples are shown in Figures 6 and 7.

At high temperatures, the reduced (excess) fugacity $(f - f_d) / f_d$ clearly influences the rate of CO_2-hydrate formation (see Fig. 6a and Table 2). During the first 6-7 hours both reactions at 253 and 263 K run closely together; only at a later stage does the reaction at 253 K significantly exceed the one at 263 K. This is due to a counterbalancing of the effects of temperature and excess fugacity. To reach the same reaction degree of 10%, a time of about 1 h is needed at 253 K; this is approximately 15 h at 230 K and exceeds 24 h at 193 K (compare Figs. 6a and 7). In all experiments the kinetic curve for the initial stage shows a strongly non-linear development in time and flattens in later stages while keeping a smooth overall shape. Our electron microscopic observations of the porous hydrate layer during stage I show that the coating process preferentially starts in cracks (see Figs. 3b, c, and d) with a subsequent spreading over the spherical grain surface. This suggests dividing stage I into two sub-stages: stage Ia (crack-filling) and stage Ib (surface-coating). The formation and spreading of hydrate patches is much slower than the filling of the cracks. Even at high temperatures, the ice surface is not fully covered with a hydrate shell after several hours, although the cracks in grains are completely filled.

Based on these observations the theoretical model described in section 3 was used to interpret the gas-consumption and diffraction data. An interactive computer program was developed to perform all necessary simulations. A least-squares procedure under user control was used to iteratively fit the model to measurements within the framework of the general strategy described at the end of section 3. The same approach was successfully employed previously in Staykova et al. (2003), and all previous simulations showed that certain parts of the kinetic curves were selectively sensitive to different groups of tuning parameters. Experimental constraints on the coating rate constants k_S and k_S^1 in Equations 3 and 6 derived from our SEM images in experiments interrupted at various temperatures were also taken into account, together with the estimate of the average crack opening angle $\beta \sim 0.06$. The most complete ice-to-hydrate conversion (up to 56%) was observed in the CO_2-D_2O clathration reaction (see Fig. 6b) at 272 K with a radius of the unreacted ice core shrunk to an averaged value of ≈ 29 μm. This makes the latter set especially valuable for model validation (Staykova et al. 2003).

The typical time scale (ω_S^{-1}) of stage I (stage Ia + stage Ib) is proportional (see Eqs. 3) to the reciprocal value of the ice-grain coating rate constant k_S^{-1} which increases from about 1 to approximately 12 h as the temperature decreases from 272 to 230 K (see Table 2). At 193 K it takes about 45 h. In these terms, for the thermodynamic driving force $\ln(f/f_d) \sim 1$, the reaction at 193 K can be interpreted as pure crack-filling during the first 5–7 h, followed by a transition period and surface-coating until approximately 150 h. The reaction curves at high temperatures are smoother, making it difficult to easily discern different sub-stages. This is in agreement with our SEM observations that at higher temperatures different stages may develop locally (grain-wise and even on one grain) with different speed and occur partly concomitantly when the whole sample is considered. As expected, the overall rates are much faster and complete surface coating at 272 K takes only about 6 h.

In all CO_2 experiments presented here the surface-coating stage was sufficiently well developed to obtain reliable values for the coating rate constant k_S. Thus, we are able to extract the activation energy Q_S of this process (see Fig. 8a). Obviously, two different regions can be considered, above and below 220–230 K. For the high temperature region, the value of the activation energy is 31.5 kJ/mol while it is 5.5 kJ/mol for the lower range. At low temperatures, the formation reactions should be followed for several months in order to get a robust result for the reaction rate constant k_R and/or permeation coefficient D. Such long-term experiments have not yet been completed and will be presented elsewhere. Nevertheless, at higher temperatures the reactions definitely reach stages II and/or III and allow for a reliable model interpretation, although, as discussed by Staykova et al. (2003), the reaction degree is still too low to distinguish between the controlling steps. The values of the reaction rate constant k_R and permeation coefficient D deduced under the assumption that the hydrate formation is either limited by reaction or diffusion are given in Table 2. They should be considered as lower estimates of these parameters if both steps are equally presented in the clathration process. The activation energy of the diffusion-limited process obtained for the 223 to 272 K range is 54.6 kJ/mol (Fig. 8b), while for the reaction-limited process an energy of 42.3 kJ/mol results from our analysis (Fig. 8c). The inferred permeation coefficient of the gas- and water-mass transfer in CO_2-hydrate formed from deuterated ice-powder is 6.4×10^{-12} m^2/h at 272 K, and is in good agreement with the estimate of about 8×10^{-16} m^2/s (3×10^{-12} m^2/h) obtained by Takeya et al. (2000) at 269 K for H_2O ice. This provides additional evidence that the isotopic properties of ice do not significantly affect gas hydrate growth and that the observed kinetics are similar. Unfortunately, the mean particle size in ice powders used by Henning et al. (2000) was not reported and a comparison with their experimental data cannot be made.

Concerning the initial crack-filling sub-stage, one can deduce from k_S^1 and k_R^1 listed in Table 2 that, in general, this process is more rapid at high temperatures, but the surface coverage, being several orders of magnitude slower at low temperatures, accelerates to a much higher degree and becomes hardly distinguishable from the crack-filling coverage (compare k_R^1 and k_R) at the melting

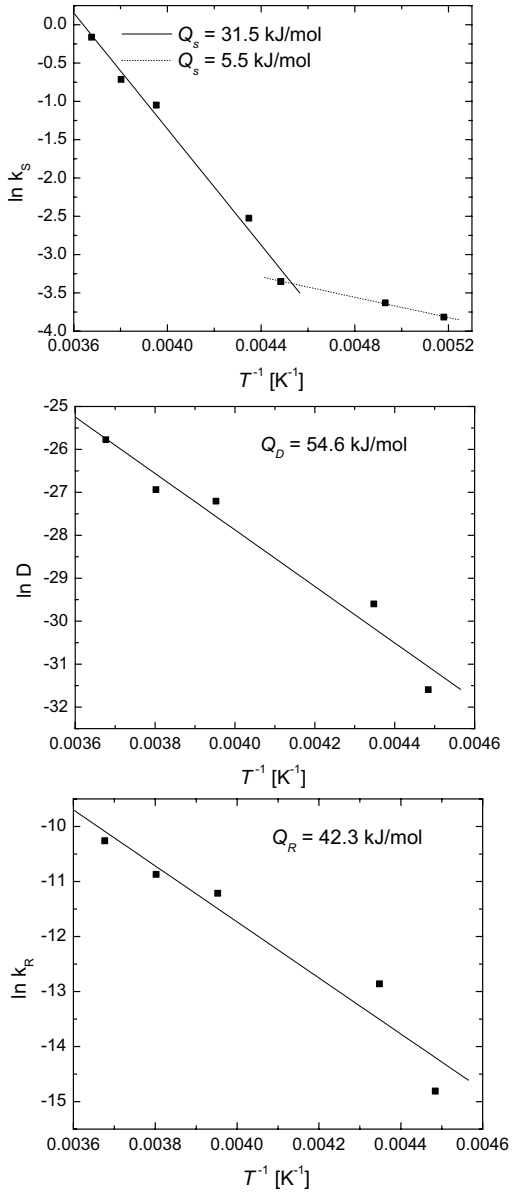

FIGURE 8. Arrhenius plots of the various stages of the CO_2 hydrate formation at temperatures above 223 K with (**a**) the surface coverage stage, (**b**) the diffusion-limited stage, and (**c**) the reaction-limited stage, as deduced from the best-fit model parameters (see Table 2).

point. This is in good agreement with our SEM observations. As a consequence, at lower temperatures the crack-filling stage is much more easily separated from a subsequent surface-coating sub-stage. From the model fits typically several μm are obtained for the thickness δ_0' of the ice layer converted to the initial hydrate film on the crack walls, which compares well with the thickness δ_0 of the coating layer on the ice grain surface, being entirely consistent with the observations from electron microscopy.

CH_4-hydrate growth from ice-powders

These experiments were reported in detail in Staykova et al. (2003). The latter paper also presented kinetic data interpretation, albeit under the assumption that ice grain surface-coating was the only process taking place in stage I of the reaction. A noticeable discrepancy between the observations and model fits at the very beginning of the kinetic curves (Staykova et al. 2003; Fig. 8) most likely was due to ignoring the crack-filling phenomenon. On the other hand, our SEM studies of methane hydrate formation suggest that at high temperatures the filling of cracks in ice grains may additionally overlap with particle necking, as well as the formation and lateral spreading of hydrate patches on the spherical ice grain surfaces. Therefore, in light of our low-temperature SEM observations when crack-filling is clearly distinguished from the much slower surface coverage, only the methane kinetic neutron data at 230 K presented in Figure 6□ have been reconsidered here. Taking into account a separate crack-filling stage improved the fit considerably and modified somewhat the remaining parameter set established in our earlier work (Staykova et al. 2003). Based on the new theoretical model we can see that this experiment was rather short and did not extend beyond stage I. Reaction and diffusion rates (parameters k_R and D) were too low to be reliably determined and are not given in Table 2. Comparison of these data in Figure 6c with those for CO_2-hydrate formation at the same temperature of 230 K allows us to estimate and compare the ice-grain coating and crack-filling rates for the CH_4- and CO_2-clathration reactions. To do this one should note that in our case (see Table 2) the excess fugacity $(f - f_d) / f_d$ for the CH_4-hydrate reaction at 230 K was about 12 times that for CO_2. Even at this much higher driving force methane reacts two to three times slower than carbon dioxide. The actual scales of the crack-filling and coating rates at equal thermodynamic conditions are characterized by the respective reaction rate constants k_S' and k_S. At 230 K (see Table 2), they are approximately one order of magnitude higher for CO_2 than for CH_4. Thus, the tendency of the clathration reaction on ice to be much slower for methane than carbon dioxide at 272 K (Staykova et al. 2003) appears to be even more pronounced at lower temperatures.

ACKNOWLEDGMENTS

The authors are grateful to L. Melesi and J.-L. Laborier (ILL, Grenoble) for their help in preparing the high pressure equipment. Likewise we thank T. Hansen (ILL, Grenoble) for his competent help in performing the D20 experiments and the ILL for beam time and support. We also thank A. Klapproth and S. Klapp (Göttingen) for discussions and help during sample preparation and data analysis. L. Legagneux and F. Dominé (LGGE, Grenoble) as well as A. Zeller (Göttingen) are gratefully acknowledged for performing the measurement of the specific surface area of the ice-powder and porous gas hydrates. This study was supported by DFG grants Ku920/9-1 and Ku920/11-1. Likewise, part of this work was supported by grant 03G0553A of the BMBF in its programme GEOTECHNOLOGIEN of which this publication is paper No. GEOTECH-56. The financial support of both DFG and BMBF is gratefully acknowledged here.

REFERENCES CITED

Arzt, E. (1982) The influence of an increasing particle coordination on the densification of spherical powders. Acta Metallurgica, 30, 1883–1890.

Aya, K., Yamane, K., and Yamada, N. (1992) Stability of clathrate hydrate of carbon dioxide in highly pressurized water. In P.E. Kroeger and Y. Bayazitogu, Eds., Fundamentals of Phase Change: Freezing, Melting, and Sublimation—1992 HTD, p. 17–22. The American Society of Mechanical Engineers, New York.

Barrer, R.M. and Edge, A.V.J. (1967) Gas hydrates containing argon, krypton and xenon: kinetics and energetics of formation and equilibria. Proceedings of the Royal Society London, A 300, 1–24.

Berliner, R., Popovici, M., Herwig, K.W., Berliner, M., Jennings, H.M., and Thomas, J.J. (1998) Quasielastic neutron scattering study of the effect of water-to-cement ration on the hydration kinetics of tricalcium silicate. Cement and Concrete Research, 28, 231–243.

Brightwell, S.N., Kargel, J.S., and Titus, T.N. (2003) Martian south polar deformation and sublimation processes. In Lunar and Planetary Science XXXIV: Papers presented to the 34th Lunar and Planetary Science Conference, March 17–21, 2003. Lunar and Planetary Institute, no. 2077, League City, Texas.

Cabrol, N.A., Grin, E.A., Landheim, R., and McKay, C.P. (1998) Cryovolcanism as a possible origin for pancake-domes in the Mars 98 landing site area: relevance for climate reconstruction and exobiology exploration. In Lunar and Planetary Science XXIX: Papers presented to the 29th Lunar and Planetary Science Conference, 16–20 March 1998. Lunar and Planetary Institute, no. 1249, Houston, Texas.

Convert, P., Hansen, T., Oed, A., and Torregrossa, J. (1998) D20 high flux two axis neutron diffractometer. Physica B, 241–243, 195–197.

Convert, P., Hansen, T., and Torregrossa, J. (2000) The high intensity two axis neutron diffractometer D20—first results. Materials Science Forum, 321–324, 314–319.

Crank, J. (1975) The Mathematics of Diffusion. Clarendon Press, Oxford.

Demirdjian, B., Ferry, D., Suzanne, J., Toubin, S., Picaud, S., Hoang, P.N.M., and Girardet, C. (2002) Structure and dynamics of ice Ih films upon HCl adsorption between 190 and 270 K. I. Neutron diffraction and quasielastic neutron scattering experiments. Journal of Chemical Physics, 116, 5143–5149.

Durham, W.B. (1998) Factors affecting the rheologic properties of Martian polar ice. First International Conference on Mars Polar Science, no. 3024.

Froment, G.F. and Bischoff, K.B. (1990) Chemical Reactor Analysis and Design. Wiley, New York.

Fujii, K. and Kondo, W. (1974) Kinetics of hydration of tricalcium silicate. Journal of the American Ceramic Society, 57, 492–497.

Henning, R.W., Schultz, A.J., Thien, V., and Halpern, Y. (2000) Neutron diffraction studies of CO_2 clathrate hydrate: formation from deuterated ice. Journal of Physical Chemistry, 104, 5066–5071.

Hondoh, T. and Uchida, T. (1992) Formation process of clathrate air-hydrate crystals in polar ice sheets. Teion Kagaku (Low Temperature Science), A51, 197–212.

Hwang, M.J., Wright, D.A., Kapur, A., and Holder, G.D. (1990) An experimental study of crystallization and crystal growth of methane hydrates from melting ice. Journal of Inclusion Phenomena, 8, 103–116.

Kargel, J.S. (1998) Possible composition of Martian polar caps and controls on ice-cap behavior. In First International Conference on Mars Polar Science: Papers presented to the First International Conference on Mars Polar Science, October 19–22, 1998. Lunar and Planetary Institute, no. 3048, Houston, Texas.

Kargel, J.S. and Tanaka, K.L. (2002) The Martian south polar cap: glacial ice sheet of multiple interbedded ices. In Lunar and Planetary Science XXXIII: Papers presented to the 33rd Lunar and Planetary Science Conference, March 11-15, 2002. Lunar and Planetary Institute, no.1799, Houston, Texas.

Klapproth, A. (2002) Strukturuntersuchungen an Methan- und Kohlenstoffdioxid-Clathrat-Hydraten. GZG, Abteilung Kristallographie. Georg-August-Universität, Göttingen.

Klapproth, A., Goreshnik, E., Staykova, D.K., Klein, H., and Kuhs, W.F. (2003) Structural studies of gas hydrates. Canadian Journal of Physics, 81, 503–518.

Komatsu, G., Kargel, J.S., Baker, V.R., Strom, R.G., Ori, G.G., Mosangini, C., and Tanaka, K.L. (2000) A chaotic terrain formation hypothesis: explosive outgas and outlow by dissociation of clathrate on Mars. In Lunar and Planetary Science XXXI: Papers presented to the 31st Lunar and Planetary Science Conference, March 13–17, 2000. Lunar and Planetary Institute, no. 1434, Houston, Texas.

Kreslavsky, M.A. and Head, J.W. (2002) Conditions and principal time scales for basal melting of Martian polar caps. Lunar and Planetary Institute, no. 1779.

Kuhs, W.F., Klapproth, A., Gotthardt, F., Techmer, K., and Heinrichs, T. (2000) The formation of meso- and macroporous gas hydrates. Geophysical Research Letters, 27, 2929–2932.

Kuhs, W.F., Genov, G., Goreshnik, E., Zeller, A., Techmer, K.S., and Bohrmann, G. (2004) The impact of porous microstructures of gas hydrates on their macroscopic properties. Proceedings of the 14th Internnational Offshore Polar Engineering Conference. ISOPE-2004, Toulon, France.

Larson, A.C. and von Dreele, R.B. (1990) Los Alamos National Laboratory. Report LAUR 86-748.

Legagneux, L., Cabanes, A., and Dominé, F. (2002) Measurement of the specific surface area of 176 snow samples using methane adsorption at 77K. Journal of Geophysical Research, 117, 4335.

Legagneux, L., Lauzier, T., Dominé, F., Kuhs, W.F., Heinrichs, T., and Techmer, K. (2003) Rate of decay of specific surface area of snow during isothermal experiments and morphological changes studied by scanning electron microscopy. Canadian Journal of Physics, 81, 459–468.

Levenspiel, O. (1999) Chemical Reaction Engineering. Wiley, New York.

Milkovich, S.M., Head, J.W., and Kreslavsky, M.A. (2002) Variations in layered deposits at the North Pole of Mars: stratigraphy along a single trough and evidence for CO_2 loss. In Lunar and Planetary Science XXXIII: Papers presented to the 33rd Lunar and Planetary Science Conference, March 4–8, 2002. Lunar and Planetary Institute, no. 1713, Houston, Texas.

Mizuno, Y. and Hanafusa, N. (1987) Studies of surface properties of ice using nuclear magnetic resonance. Journal de Physique, Colloque C1, Supplement au N3, 48, C1-511–C1-517.

Mori, Y.H. (1998) Clathrate hydrate formation at the interface between liquid CO_2 and water phases—A review of rival models characterizing "hydrate films". Energy Conversion and Management, 39, 1537–1557.

Mori, Y.H. and Mochizuki, T. (1997) Mass transport across clathrate hydrate films—a capillary permeation model. Chemical Engineering Science, 52, 3613–3616.

Salamatin, A.N. and Kuhs, W.F. (2002) Formation of porous gas hydrates. Proceedings of the Fourth International Conference on Gas Hydrates, Yokohama, May 19–23, 2002, Yokohama, p. 766–770. http://hydrate.welcome.to/pdf/ICGH766.pdf

Salamatin, A.N., Hondoh, T., Uchida, T., and Lipenkov, V.Y. (1998) Post-nucleation conversion of an air bubble to clathrate air-hydrate crystal in ice. Journal of Crystal Growth, 193, 197–218.

Sloan, E.D. Jr. (1998) Clathrate Hydrates of Natural Gases. Dekker, New York.

Sloan, E.D. Jr. and Fleyfel, F. (1991) A molecular mechanism for gas hydrate nucleation from ice. Institute of Chemical Engineering Journal, 37, 1281–1292.

Staykova, D.K., Hansen, T., Salamatin, A.N., and Kuhs, W.F. (2002) Kinetic diffraction experiments on the formation of porous gas hydrates. Proceedings of the Fourth International Conference on Gas Hydrates, Yokohama, May 19–23, 2002, 2, Yokohama, p. 537–542. http://hydrate.welcome.to/pdf/ICGH537.pdf

Staykova, D.K., Kuhs, W.F., Salamatin, A.N., and Hansen, T. (2003) Formation of porous gas hydrates from ice powders: Diffraction experiments and multi-stage model. Journal of Physical Chemistry B, 107, 10299–10311.

Stern, L.A., Hogenboom, D.L., Durham, W.B., Kirby, S.H., and Chou, I.M. (1998) Optical-cell evidence for superheated ice under gas-hydrate-forming conditions. Journal of Physical Chemistry B, 102, 2627–2632.

Suess, E., Bohrmann, G., Rickert, D., Kuhs, W.F., Torres, M.E., Trehu, A., and Linke, P. (2002) Properties and fabric of near-surface methane hydrates at Hydrate Ridge, Cascadia Margin. Proceedings of the Fourth International Conference on Gas Hydrates, Yokohama, May 19–23, 2002, Yokohama, p. 740–744. http://hydrate.welcome.to/pdf/ICGH740.pdf

Sugaya, M. and Mori, Y.H. (1996) Behavior of clathrate hydrate formation at the boundary of liquid water and fluorocarbon in liquid or vapor state. Chemical Engineering Science, 51, 3505–3517.

Takeya, S., Hondoh, T., and Uchida, T. (2000) In-situ observations of CO_2 hydrate by X-ray diffraction. Annals of the New York Academy of Sciences, 912, 973–982.

Takeya, S., Shimada, W., Kamata, Y., Ebinuma, T., Uchida, T., Nagao, J., and Narita, H. (2001) In situ X-ray diffraction measurements of the self-preservation effect of CH_4 hydrate. Journal of Physical Chemistry A, 105, 9756–9759.

Toubin, C., Picaud, S., Hoang, P.N.M., Girardet, C., Demirdjian, B., Ferry, D., and Suzanne, J. (2002) Structure and dynamics of ice Ih films upon HCl adsorption between 190 and 270 K. II. Molecular dynamics simulations. Journal of Chemical Physics, 116, 5150–5157.

Uchida, T. and Kawabata, J. (1995) Observations of water droplets in liquid carbon dioxide. Proceedings of the MARIENV 95 Conference, September 1995, Tokyo, p. 906–910.

Uchida, T., Hondoh, T., Mae, S., Duval, P., and Lipenkov, V.Y. (1992) In-situ observations of growth process of clathrate air-hydrate under hydrostatic pressure. In N. Maeno and T. Hondoh, Eds., Physics and Chemistry of Ice, p. 121–125. Hokkaido University Press, Sapporo.

——— (1994) Effects of temperature and pressure on transformation rate from air-bubbles to air-hydrate crystals in ice sheets. Annals of Glaciology, 20, 143–147.

van der Waals, J.H. and Platteeuw, J.C. (1959) Clathrate solutions. Advances in Chemical Physics, 2, 1–57.

Wang, X., Schultz, A.J., and Halpern, Y. (2002) Kinetics of ice particle conversion to methane hydrate. Proceedings of the Fourth International Conference on Gas Hydrates, Yokohama, May 19–23, 2002. Yokohama, p. 455–460.

Warzinski, R.P., Lynn, R.J., and Holder, G.D. (2000) The impact of CO_2 clathrate hydrate on deep ocean sequestration of CO_2. Annals of the New York Academy of Sciences, 912, 226–234.

Wilson, L. and Head, J.W. (2002) Volcanic eruption styles on Mars due to shallow interactions between magma and volatiles. In Lunar and Planetary Science XXXI : Papers presented to the 31st Lunar and Planetary Science Conference, March 13-17, 2000, Houston, Texas, Lunar and Planetary Institute, no. 1275.

Manuscript received October 3, 2003
Manuscript accepted April 21, 2004
Manuscript handled by Bryan Chakoumakos

see appendices next page

APPENDIX A. SAMPLE STRUCTURE DESCRIPTION

As suggested by Arzt (1982), in random dense packing without particle rearrangement, the current coordination number Z can be expressed as a linear function of the relative hydrate shell radius $R_h = r_h/r_{i0}$:

$$Z = Z_0 + C(R_h - 1) \tag{A1}$$

where the coordination number of the initial ice-powder $Z_0 \sim 7$, and the slope of the random density function $C \sim 15.5$.

The normalized volume of a reference ice-hydrate particle schematically depicted in Figure 4 is directly related (Arzt 1982) to the relative ice-core radius $R_i = r_i/r_{i0}$

$$R_h^3 - \frac{Z_0}{4}\left(R_h - 1\right)^2\left(2R_h + 1\right) - \frac{C}{16}\left(R_h - 1\right)^3\left(3R_h + 1\right) = 1 + E\left(1 - R_i^3\right) \tag{A2}$$

The fraction s of the free hydrate surface area (in units of $4\pi r_h^2$) exposed to the ambient gas is (Arzt 1982)

$$s = 1 - \frac{Z_0}{2}\frac{R_h - 1}{R_h} - \frac{C}{4}\frac{\left(R_h - 1\right)^2}{R_h} \tag{A3}$$

The geometrical model A1–A3 fully describes the sample packing development during the ice to hydrate conversion. The initial macro-porosity of the ice-powder ε_{m0} is directly linked to the packing parameters Z_0 and C in Equation A1, the quantity $(1 - \varepsilon_{m0})^{-1}$ being equal to the maximum normalized volume of the reference ice-hydrate particle, i.e., to the value of the left-hand side of Equation A2 at $s = 0$ in Equation A3. Accordingly, the current porosity ε_m and the normalized surface area of the macro-pore space are

$$\varepsilon_m = \varepsilon_{m0} - E(1 - \varepsilon_{m0})(1\ R_i^3), \quad S_m = sR_h^2 S_{i0}.$$

The area of the spherical cap surface of radius r_h cut by one average contact from the truncated hydrate shell in Figure 4 can be calculated in two different ways:

$$2\pi r_h(r_h - r) = 4\pi r_h^2(1–s)/Z$$

thus yielding the distance r from the ice core center to an average contact plane

$$r = r_h\left[1 - \frac{2(1-s)}{Z}\right]$$

APPENDIX B. GAS HYDRATE FORMATION IN A CRACK

We assume that on average the initial fissure in a reference ice grain of radius r_0 has the form of a cleft penetrating to the sphere center with the angle 2β between its sides S_f (see Fig. 5). Most probably due to numerous physical defects, the process of gas hydrate formation in the cracks is much faster in comparison with the growth of hydrate layers around the shrinking ice cores. Nevertheless, SEM observations show that in general the crack-filling passes through the two analogous stages of (1) hydrate film coating the crack surface and (2) reaction-controlled growth of the hydrate layer on the two crack sides. Thus, per unit time, additional fraction $\omega'_S e^{-\omega'_S t}$ of the crack surface is covered with the initial hydrate film, formed of an ice layer with thickness δ'_0, and on the coated area exposed to the ambient gas, the ice layer of ω'_R/ρ_i-thickness transforms to hydrate. In each case, the newly formed porous hydrate layer is $1 + E$ times thicker than the consumed ice. The incremental excess hydrate volume intrudes into the cleft from both sides and leads to an increase in the average height h of the crack-filling. The above process is governed by an equation that copies Equation 2_2

$$\beta\frac{dh}{dt} = E\delta'_0\omega'_S e^{-\omega'_S t} + E\frac{\omega'_R}{\rho_i}\left(1 - e^{-\omega'_S t}\right)$$

and results in Equation 6_1.

Simultaneously, the cleavage-side area (initially equal to $\pi r_0^2/2$) decreases

$$\frac{dS_f}{dh} = -2\sqrt{r_0^2 - h^2},$$

whereas the hydrate volume v_f formed in and around the crack increases

$$\frac{dv_f}{dh} = 2\beta S_f\frac{1+E}{E}.$$

The sequential integration of the latter equations with respect to h from 0 to h yields

$$S_f = \frac{\pi r_0^2}{2}\left(1 - \frac{2}{\pi}\arcsin\frac{h}{r_0}\right) - h\sqrt{r_0^2 - h^2}$$

and

$$v_f = 2\beta r_0^3\frac{1+E}{E}\left[\frac{\pi}{2}\xi - \xi\arcsin\xi - \left(1-\xi^2\right)^{1/2} + \frac{1}{3}\left(1-\xi^2\right)^{3/2} + \frac{2}{3}\right],\ \xi = h/r_0.$$

The total hydrate volume which completely fills the crack corresponds to $\xi = 1$, and the last relation determines the current filling degree $\chi = v_f/v_f(\xi = 1)$ given by Equation 6_2.